Study on dislocation behavior in a polycrystalline Mg-Y alloy using multi-scale characterization and VPSC simulation

Bijin Zhou[a,b,c], Leyun Wang[a,f*], Jinhui Wang[d], Alireza Maldar[a], Gaoming Zhu[a], Hailong Jia[e], Peipeng Jin[d], Xiaoqin Zeng[a,f*], Yanjun Li[c*]

[a]*National Engineering Research Center of Light Alloy Net Forming, Shanghai Jiao Tong University, Shanghai 200240, China*

[b]*School of Mechanical Engineering, Suzhou University of Science and Technology, Suzhou 215009, China*

[c]*Department of Materials Science and Engineering, Norwegian University of Science and Technology, Trondheim 7491, Norway*

[d]*School of Mechanical Engineering, Qinghai University, Xining 810016, China*

[e]*Key Laboratory of Automobile Materials of Ministry of Education & School of Materials Science and Engineering, Nanling Campus, Jilin University, Changchun 130025, China*

[f]*State Key Laboratory of Metal Matrix Composites, Shanghai Jiao Tong University, Shanghai 200240, China*

*Corresponding author: yanjun.li@ntnu.no, xqzeng@sjtu.edu.cn, and leyunwang@sjtu.edu.cn

Abstract

In this study, the dislocation behavior of a polycrystalline Mg-5Y alloy during tensile deformation were quantitatively studied by an in-situ tensile test, visco-plastic self-consistent (VPSC) modeling, and TEM. The results show that 〈a〉 dislocations contribute to most of the deformation, while a small fraction of 〈c+a〉 dislocations are also activated at near grain boundaries (GBs) regions. The critical resolved shear stresses (CRSSs) of different dislocation slip systems were estimated. The CRSS ratio between prismatic and basal 〈a〉 dislocation slip in the Mg-Y alloy (~13) is lower than that of pure Mg (~80), which is considered as a major reason for the high ductility of the alloy. TEM study shows that the 〈c+a〉 dislocations in the alloy have a high mobility, which also helps to to accommodate the deformation near GBs.

Keywords: Mg-Y alloy; dislocation behavior; deformation mechanisms; critical

resolved shear stress

1. Introduction

As the lightest metallic structural material and with big application potential in aerospace and automotive industries [1, 2], magnesium (Mg) and its alloys have received strong attention. Nevertheless, due to the limited slip system activated during deformation, pure Mg and some commercial Mg alloys (e.g., Mg-3Al-1Zn (AZ31)) have relatively low ductility and formability, which have hindered their broader applications [3].

It has been found that alloying by yttrium (Y) can improve the plasticity of Mg alloys [4-9]. Sandlöbes et al. [4] reported that a Mg-3Y (wt.%) alloy develops a weak basal-type texture after rolling and heat treatment, with most grains having their basal plane (0001) deviate to the rolling plane. Compared to pure Mg (~4%) with strong basal-type textures, the Mg-3Y alloy shows a distinctively higher tensile elongation (~25%). The good ductility of Mg-Y alloys, therefore, has been correlated with the weakened deformation texture by Y [1, 4, 10].

The effect of Y on the dislocation behavior of Mg plays a key factor as well [5, 11-17]. Several works regarded the effect of Y on the 〈c+a〉 dislocation mobility as the main mechanism behind [12, 14, 18, 19]. For example, according to the results of atomistic simulations, Wu and Curtin et al. [12, 20] reported that the cross-slip energy barrier of the 〈c+a〉 dislocation from the pyramidal II to pyramidal I plane in Mg can be reduced by an appropriate Y addition. The reduction caused the cross-slip of 〈c+a〉 screw dislocations to become the main mode of 〈c+a〉 dislocation movement. Effective deformation can be generated by the 〈c+a〉 cross-slip, which leads to continuous dislocation multiplication [11, 12, 21]. Y was also supposed to strengthen the basal 〈a〉 dislocation slip in Mg-Y alloys, leading to a lower critical resolved shear stress (CRSS) ratio between non-basal and basal dislocation slip [13, 16, 22, 23]. Kim et al. [13] investigated the effect of Y on the CRSS values of different dislocation slip in Mg using molecular dynamics simulation, where the results showed that Y reinforces basal 〈a〉 dislocation slip more than ⟨c+a⟩ dislocation slip. This can reduce the activation gap between non-basal slip and basal ⟨a⟩ slip. However, it is yet to reveal whether the Y-increased mobility of ⟨c+a⟩ dislocation or the Y-strengthened basal ⟨a⟩ slip plays more important roles in the high ductility of Mg-Y alloys. This can help to reach an in-depth understanding on the mechanisms of ductility improvement of Mg alloys.

Thus, this work examines the dislocation activities in Mg-Y alloys using in-situ EBSD/SEM, VPSC simulation, and TEM. The microstructure of a Mg-5Y alloy was first characterized at different strains by EBSD/SEM. Then the ***intragranular*** slip traces and the slip traces ***near*** grain boundaries (GBs) were investigated separately. The VPSC modeling was carried out based on the in-situ test results, including the microstructure evolution, the stress-strain curve, and the measured CRSSs. TEM observation was also used to examine detailed dislocation behavior.

2. Experimental and modeling procedures

2.1 Sample preparation and characterization

The material used in this work was an extruded Mg-5Y (wt.%) alloy and its process history has been reported previously [24]. A sample with nominal gauge dimensions of 11 mm (L) × 4 mm (W) × 1.4 mm (T) was fabricated by electron discharge machining for an in-situ tensile test, with the tensile direction (TD) being parallel to the extrusion direction (ED). The sample was electro-polished in an ethanol solution containing 10 vol.% perchloric at 30 V and -30 °C for 150 s. The in-situ tensile test was conducted at room temperature in a SEM (ZEISS, Merlin compact) equipped with an EBSD detector (Oxford, NordlysMax^2) and a commercial testing module (Deben, Microtester 2 kN). The crosshead speed was 0.4 mm·min^{-1}, equivalent to a nominal strain rate of 6.0×10^{-4} s^{-1}. SEM was conducted to image the microstructures at strains of 0%, 1.6%, 4.4%, 6.4%, 8.8%, and 12.8%. After each SEM image collection, except for 6.4% strain, the orientation data at different strains was obtained by EBSD characterization. To optimize the quality of EBSD imaging and the acquisition time, operating voltage of 20 kV and scan step sizes of 0.5 and 1.0 μm were chosen for the EBSD scan. The EBSD data were analyzed by ATEX software v2.01 (http://www.atex-software.eu/) and OIM Analysis™

v7.0.

TEM samples were prepared in an ethanol solution containing 4 vol.% perchloric acid at 35 V and -40 °C using twin-jet electropolishing (Struers, TenuPol-5). A JEOL-2100F instrument was operated to image dislocations in grains at working voltage of 200 kV.

2.2 Determination of dislocation slip types by lattice rotation analysis

Since the conventional slip trace analysis can only provide limited information of slip planes [25-27], in this work, a recently developed EBSD-based lattice rotation analysis was used to determine the types of observed slip traces [24, 28]. Fig. 1 provides an example for identifying the basal slip system and the pyramidal I slip system. Fig. 1a and 1b show the inverse pole figure (IPF) map and the corresponding SEM image of a region of interest. There are two kinds of surface slip traces in Grain A (Average Euler angle = (216°, 15°, 314°)). Fig. 1c shows the simulated slip traces of 30 possible slip systems in the grain (basal ⟨a⟩: 1-3; prismatic ⟨a⟩: 4-6; pyramidal I ⟨a⟩: 7-12; pyramidal I ⟨c+a⟩: 13-24; pyramidal II ⟨c+a⟩: 25-30). A comparison of the observed slip traces and the simulated slip traces infers that the basal (0001) slip and the pyramidal I $(\bar{1}011)$ slip systems were activated. Note that it is difficult to identify their specific Burgers vectors because all the three basal (i.e., 1, 2, and 3) slip systems share the same simulated basal slip trace while three pyramidal I (i.e., 7, 13, and 14) slip systems share the same pyramidal I plane slip trace. In such situations, the Burgers vectors of the two slip systems can be determined based on the long-range intragranular misorientation of Grain A. Fig. 1d shows the {0002} pole figure of Grain A. An enlarged image of the (0002) pole shows that the (0002) pole is stretched along two directions, which represents the lattice rotation of Grain A. Two rotation axes were determined as $\sim[10\bar{1}0]$ and $\sim[\bar{1}2\bar{1}0]$, respectively, indicating that the slip systems $(0001)[\bar{1}2\bar{1}0]$ and $(\bar{1}011)[\bar{1}\bar{1}2\bar{3}]$ were activated in Grain A. The same analysis was carried out for all the observed slip traces at each deformation step.

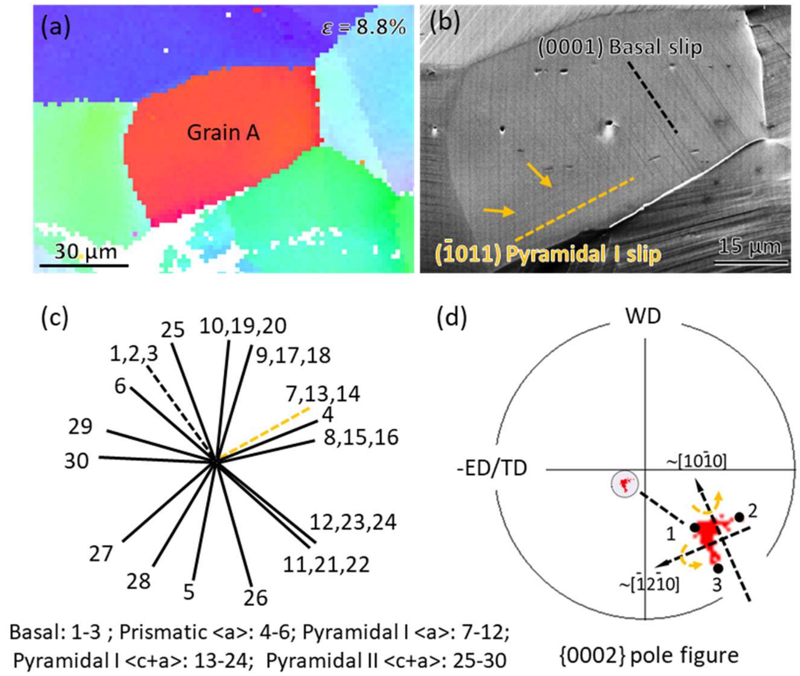

Figure 1. Identification for the activated slip systems by slip trace and lattice rotation analysis. (a) Inverse pole figure (IPF) map of Grain A and its neighboring grains. (b) SEM image showing two kinds of surface slip traces in Grain A. (c) 30 simulated slip traces of Grain A. (d){0002}pole figure of Grain A. The (0002) pole was stretched along two directions: the streak from 1 to 2 is caused by the basal ⟨a⟩ dislocation slip; the streak from 1 to 3 is caused by the pyramidal I ⟨c+a⟩ dislocation slip.

2.3 VPSC modeling

In this study, the threshold stress (τ^s) for each slip system (s) increasing with accumulated shear strain (Γ) is described by an extended Voce equation:

$$\tau^s = \tau_0^s + (\tau_1^s + \theta_1^s \Gamma)\left(1 - \exp\left(-\Gamma\left|\frac{\theta_0^s}{\tau_1^s}\right|\right)\right) \quad (1)$$

In the standard VPSC simulation, τ_0^s, $(\tau_0^s + \tau_1^s)$, θ_0^s, and θ_1^s are the fundamental CRSS, the back-extrapolated threshold stress, the initial hardening rate, and the asymptotic hardening rate of each deformation mode, respectively. When involving 5 deformation modes, at least 20 material parameters should be adjusted. Verifying such a large number of material parameters is not an easy task.

In our work, a simplified approach to VPSC modeling, proposed by Hutchinson et al. [29], was adopted. The assumption in Hutchinson's work is that τ_0^s indeed involves two parts: the fundamental CRSS and a microstructure-related constant (τ_c). The latter part derives from the effect of grain boundaries and/or precipitates. Furthermore, for all deformation modes, τ_c, τ_1^s, θ_0^s, and θ_1^s were assumed to be constants. This approach immensely reduces the number of adjustable parameters and has been successfully used to predict the complex plastic behavior of AZ31 alloys [29, 30].

The initial grain orientations and grain geometry information of 224 grains in the Mg-5Y alloy were used as input data for the VPSC modeling. Five deformation modes, namely basal ⟨a⟩, prismatic ⟨a⟩, pyramidal I ⟨a⟩, pyramidal I ⟨c+a⟩, and pyramidal II ⟨c+a⟩ were included in the simulation. The fundamental CRSSs of different slip modes were depended on the experimental CRSSs estimated from the in-situ tensile test. The remaining four parameters (i.e., τ_c, τ_1^s, θ_0^s, and θ_1^s) were determined by trial and error when a good agreement between the simulated and the experimental results was obtained.

3. Results

3.1 Initial microstructure

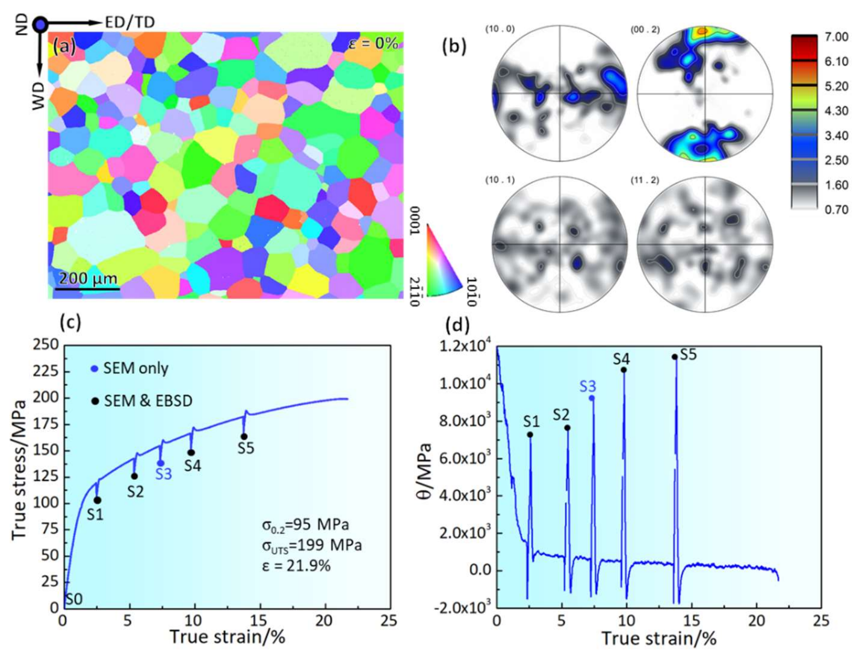

Figure 2. (a) IPF map of the region of interest before deformation. (b) Pole figures corresponding to (a). (c) True stress-true strain curve of the in-situ tensile test during which the SEM/EBSD imaging was conducted at 0% (S0), 1.6% (S1), 4.4% (S2), 6.8% (S3, SEM only), 8.8% (S4), and 12.8% (S5) strains. (d) Work hardening curve corresponding to the true strain-true stress curve presented in (c). The monotonic decrease of the work hardening response was interrupted during the in-situ test.

Fig. 2a and 2b show the microstructure of the Mg-5Y alloy before tensile deformation. The IPF map of a region with area of 900 μm × 1140 μm (Fig. 2a) and the corresponding $\{10\bar{1}0\}$, $\{0002\}$, $\{10\bar{1}1\}$, and $\{11\bar{2}2\}$ pole figures (Fig. 2b) are presented. The alloy has a near-equiaxed grain structure with average grain size of ~96 μm. Because of the addition of Y, the maximum intensity of the texture component shown in the $\{0002\}$ pole figure is 5.41 mrd, a value much lower than in some extruded Y-free Mg alloys' [31-33]. A comparison among the four pole figures indicates that the sample has a less favorable orientation for basal dislocation slip than for non-basal dislocation slip. The average macro Schmid Factors (SFs) of the basal ⟨a⟩, prismatic ⟨a⟩, pyramidal I ⟨a⟩, pyramidal I ⟨c+a⟩, and pyramidal II ⟨c+a⟩ dislocation slip in all the grains were calculated as 0.275, 0.397, 0.445, 0.449, and 0.409, respectively.

3.2 Tensile deformation at room temperature

3.2.1 Mechanical properties and microstructure evolution

The true stress-true strain curve of the Mg-Y alloy obtained from the in-situ tensile test is shown in Fig. 2c. The 0.2% offset tensile yield stress ($\sigma_{0.2}$) and the ultimate tensile stress (σ_{UTS}) are 95 MPa and 199 MPa, respectively. As the loading reached the ultimate tensile stress, the sample failed at a strain of 21.9%. Stress drops occurred at each probed strain because of the stress relaxation occurring when the tests were paused for SEM and EBSD imaging. The work hardening curve calculated from the data in Fig. 2c is presented in Fig. 2d. A monotonic decrease of the work hardening rate is apparent , which implies that no distinct extension twinning occurred during the deformation [35, 36].

The grain orientation evolution of the Mg-Y alloy with increasing tensile strain is presented in Fig. 3. There is no obvious change for the orientation of these grains, showing that twinning is limited (~1.0% in area fraction) before the 12.8% strain. The low activity of extension twins can be ascribed to the Y addition and the feature of the extruded texture that most grains are oriented with their *c*-axis nearly perpendicular to the tensile direction [37]. Because the twin volume of the deformed Mg-Y sample is small, the dislocation behavior focused in this study is under little influence of twinning.

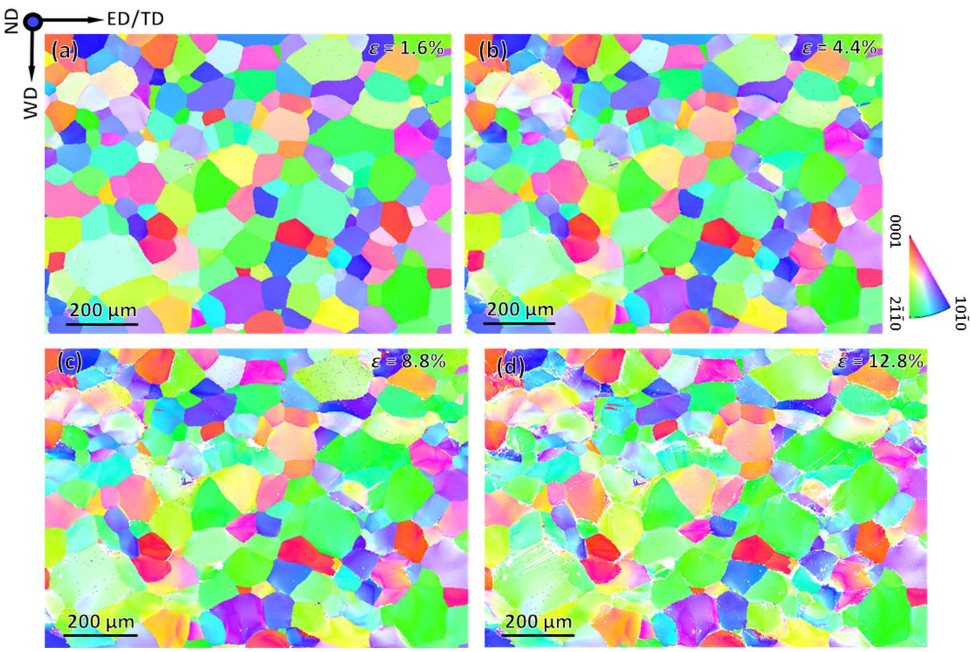

Figure 3. IPF maps showing microstructure evolution with tensile strain.

3.2.2 Non-basal dislocation behavior within grains and near grain boundaries

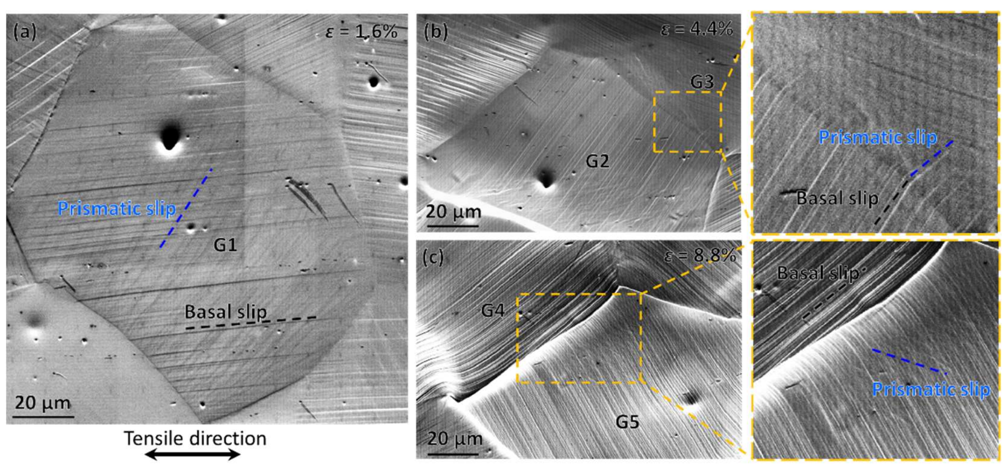

Figure 4. Typical morphologies of (a) ***intragranular*** non-basal slip traces and (b-c) non-basal slip traces ***near*** GBs.

Almost all grains (216 out of 224) developed intragranular basal slip traces even at 1.6% true strain. Fig. 4a shows the slip traces within grain G1 at 1.6% strain. The slip traces nearly parallel to the TD were determined to be basal slip by slip trace analysis; the slip traces with an approximately 60° angle to the basal slip traces were from prismatic slip. Fig. 4b shows that grain G2 is dominated by basal dislocation slip at 4.4% strain. In grain G3, prismatic slip has been triggered by the basal dislocation slip in grain G2. Fig. 4c shows another type of dislocation slip near GBs: a prismatic slip system was locally activated near the GB.

To obtain statistic, the non-basal dislocation slip traces ***inside*** grains (such as the prismatic slip in Fig. 4a) and ***near*** GBs (such as the prismatic slip in Fig. 4b and 4c) were analyzed at each probed strain for all of the 224 grains in Fig. 2a. As seen in Table 1, ***intragranular*** non-basal slip traces are observed in 65, 117, 141, 145, and 155 grains at 1.6%, 4.4%, 6.8%, 8.8%, and 12.8% strains, respectively. Non-basal slip traces ***near*** GBs are observed in 54, 81, 92, 94, and 97 grains, respectively. Note that if a grain contains more than one type of slip trace, then each type is counted once in Table 1.This table shows that prismatic ⟨a⟩ dislocation slip is more dominant than the non-basal dislocation slip. The is in agreement with the results of the previous works [7, 38]. The statistics in Table 1 also indicates that the fraction of non-basal dislocation slip near GBs is comparable to that of the intragranular non-basal dislocation slip. Furthermore, it can be inferred that GBs promotes the activation of the pyramidal I ⟨a⟩, pyramidal I ⟨c+a⟩, and pyramidal II ⟨c+a⟩ dislocation slip at the preliminary stage of the tensile deformation. For example, at 1.6% strain, the pyramidal I ⟨a⟩, pyramidal I ⟨c+a⟩, and pyramidal II ⟨c+a⟩ slip traces are observed near 21, 8, and 11 GBs at 1.6% strain, while only 9, 1, and 3 grains develop the intragranular pyramidal I ⟨a⟩, pyramidal I ⟨c+a⟩, and pyramidal II ⟨c+a⟩ dislocation slip, respectively.

Table 1. Slip activity (inside grains and near GBs) for the Mg-5Y sample at various strains.

Strain	Slip modes (inside grains/near GBs)				
	Pris. ⟨a⟩	Pyra. ⟨a⟩	Pyra. I ⟨c+a⟩	Pyra. II ⟨c+a⟩	Total
1.6%	52/14	9/21	1/8	3/11	65/54
4.4%	77/27	26/27	6/11	8/16	117/81
6.8%	92/32	29/32	7/11	13/17	141/92
8.8%	93/33	31/33	7/11	14/17	145/94
12.8%	97/33	33/33	8/14	17/17	155/97

The fraction of grains with the non-basal slip mode at each deformation strain has been calculated as well. Fig. 5a shows that the frequency of the intragranular prismatic ⟨a⟩ dislocation slip is significantly higher than other intragranular non-basal dislocation slip, suggesting that the CRSS of prismatic ⟨a⟩ dislocation slip is lower than that of other types of non-basal dislocation slip in Mg-Y alloy [23]. However, the difference in the proportion of different non-basal dislocation slip observed near GB is much smaller (Fig. 5b), which indicates that the activation of the non-basal dislocation slip around GBs is less sensitive to the macro stress. The stress concentration near GBs could play an important role in non-basal dislocation nucleation [39].

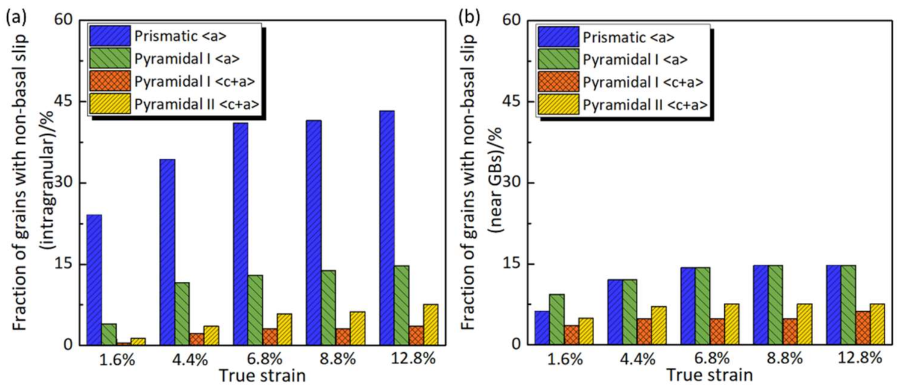

Figure 5. Proportion of grains showing the non-basal dislocation slip traces at different strains for the Mg-5Y alloy. (a) Slip traces inside grains and (b) slip traces near GBs.

Among different slip systems of a slip mode, if the one with the largest SF is activated, its activation is always regarded as obeying the Schmid criterion. Conversely, if the observed dislocation slip system does not have the largest SF, the activation cannot be ascribed merely to the macro stress. To evaluate whether the non-basal dislocation slip follow the Schmid criterion or not, the SF of the observed non-basal dislocation slip ($SF_{observed}$) and the maximum SF (SF_{max}) of the corresponding slip mode were calculated. Fig. 6a presents the relationship between $SF_{observed}$ and SF_{max} for the intragranular non-basal dislocation slip at 1.6% strain. When $SF_{observed}$ and SF_{max} are the same, data points will be located on the dashed lines. After a close examination, it is found that most of data points (43 of 52 prismatic ⟨a⟩; 6 of 9 pyramidal I ⟨a⟩; 1 of 1 pyramidal I ⟨c+a⟩; 1 of 3 pyramidal II ⟨c+a⟩) in Fig. 6a were on the dashed line. Fig. 6b shows the relationship between $SF_{observed}$ and SF_{max} for non-basal dislocation slip near GBs at 1.6% strain. Much fewer data points (7 of 14 prismatic ⟨a⟩; 6 of 21 pyramidal I ⟨a⟩; 2 of 8 pyramidal I ⟨c+a⟩; 3 of 11 pyramidal II ⟨c+a⟩) in Fig. 6b are on the dashed line. A comparison of Fig. 6a and 6b indicates that the activation of most of the intragranular non-basal slip follows the Schmid criterion, whereas only a small fraction of the activated dislocation slip near GBs follows the Schmid criterion. This confirms that the stress concentration or strain incompatibility near GBs significantly affects non-basal dislocation nucleation during deformation.

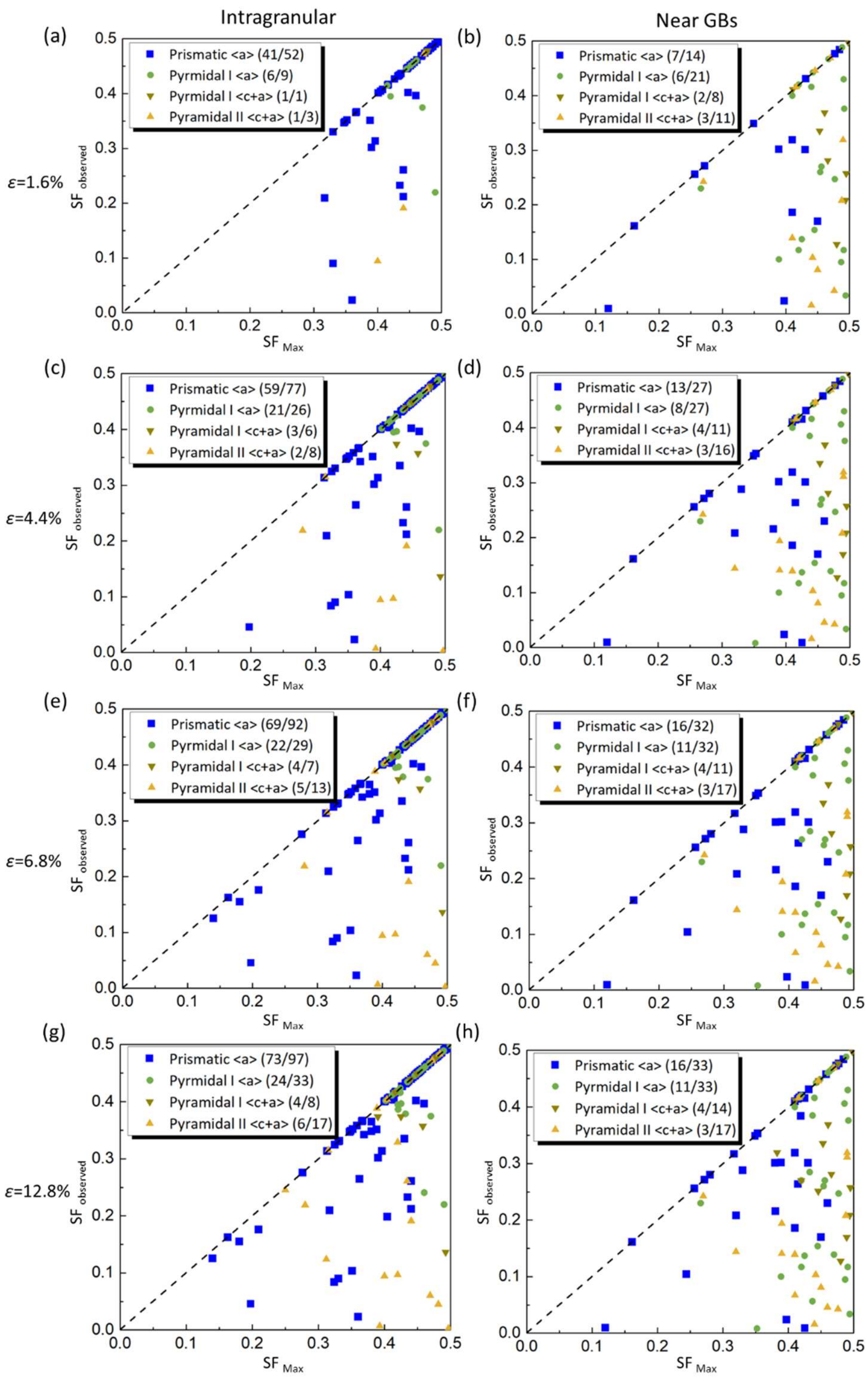

Figure 6. Schmid Factors of the activated non-basal dislocation slip ($SF_{observed}$) in comparison to the maximum SFs (SF_{max}) of the corresponding non-basal slip modes at four strains (in the four rows). The left

column presents the observed slips within the grains. The right column presents the the observed slips within the grains near GBs, showing that most of the slip near GBs does not follow the Schmid law.

Fig. 6c and 6d show the calculated SF values of the activated non-basal dislocation slip in comparison to the maximum SF values of the same slip mode at 4.4% strain. ~72% of the observed intragranular non-basal dislocation slip has the largest SF, while only ~35% of the non-basal slip activation near GBs shows a correlation with the Schmid criterion. The same tendency is also observed at higher strains (i.e., 6.8% and 12.8%), as shown in Fig. 6e-6h.

3.2.3 CRSS estimation for the intragranular dislocation slip

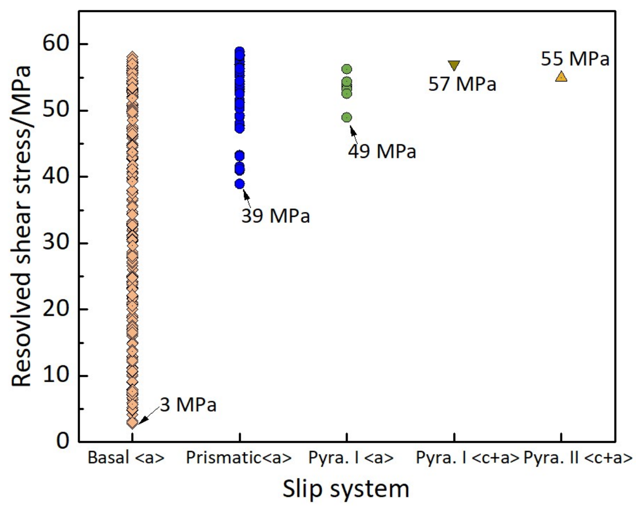

Figure 7. Experimentally determined shear stresses of the activated dislocation slip in the Mg-5Y alloy.

Assuming that the micro stress of each grain is equal to the macro stress of the tensile sample, the resolved shear stresses (τ) acting on the activated intragranular slip system can be obtained by $\tau = \sigma \cdot SF_{observed}$, where σ is the applied macro stress [40]. Here, the determination for τ is based on the observed ***intragranular*** slip systems that ***follow the Schmid criterion***. Under such conditions, the deformation of these grains was more likely controlled by the macro stress. Fig. 7 shows the distribution of the τ values of the activated slip systems at the macro stress of 118 MPa, corresponding to 1.6% strain. By using the minimum resolved shear stress, the CRSS values for the basal 〈a〉, prismatic 〈a〉, pyramidal I 〈a〉, pyramidal I 〈c+a〉, and pyramidal II 〈c+a〉 dislocation slip are calculated as 3 MPa, 39 MPa, 49 MPa, 57 MPa, and 55 MPa, respectively.

3.3 VPSC simulation

VPSC modeling based on the in-situ test is a good method to further quantify the relative activities of different deformation modes. The true stress-true strain curve simulated by the VPSC model is shown in Fig. 8. A good agreement between the simulated and experimental strain-stress curves was obtained after a dozen of trials to calibrate the material parameters: fundamental CRSSs, τ_c, τ_1^s, θ_0^s, and θ_1^s. The parameters used for the simulation are listed in Table 2. As shown, the CRSS values are quite close to the measured values. Fig. 9 compares the simulated deformation texture with the experimental measurement. At different strains, the simulated pole figures show a good agreement with the experimental results.

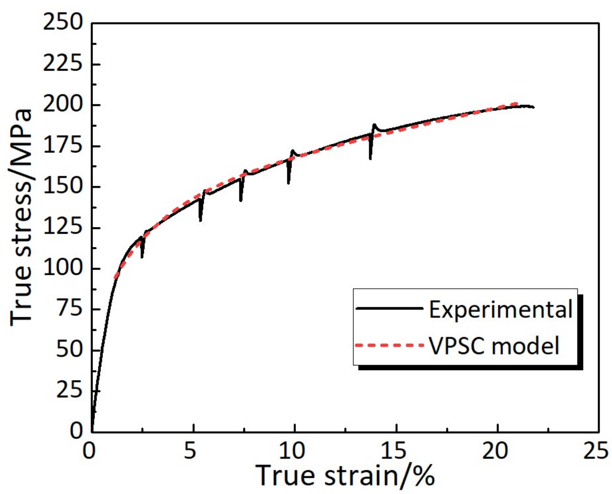

Figure 8. Comparison of the simulated true stress-strain curve (the dashed line) by the VPSC simulation and the one (the solid line) by the in-situ tensile test shows very close agreement.

Table 2. Material parameters of the Mg-5Y alloy used in the VPSC modeling (MPa).

Fundamental CRSSs					Adjustable parameters			
Basal <a>	Pris. <a>	Pyra. I <a>	Pyra. I <c+a>	Pyra. II <c+a>	τ_c	τ_1^s	θ_0^s	θ_1^s
2	41	51	72	62	8	15	240	48

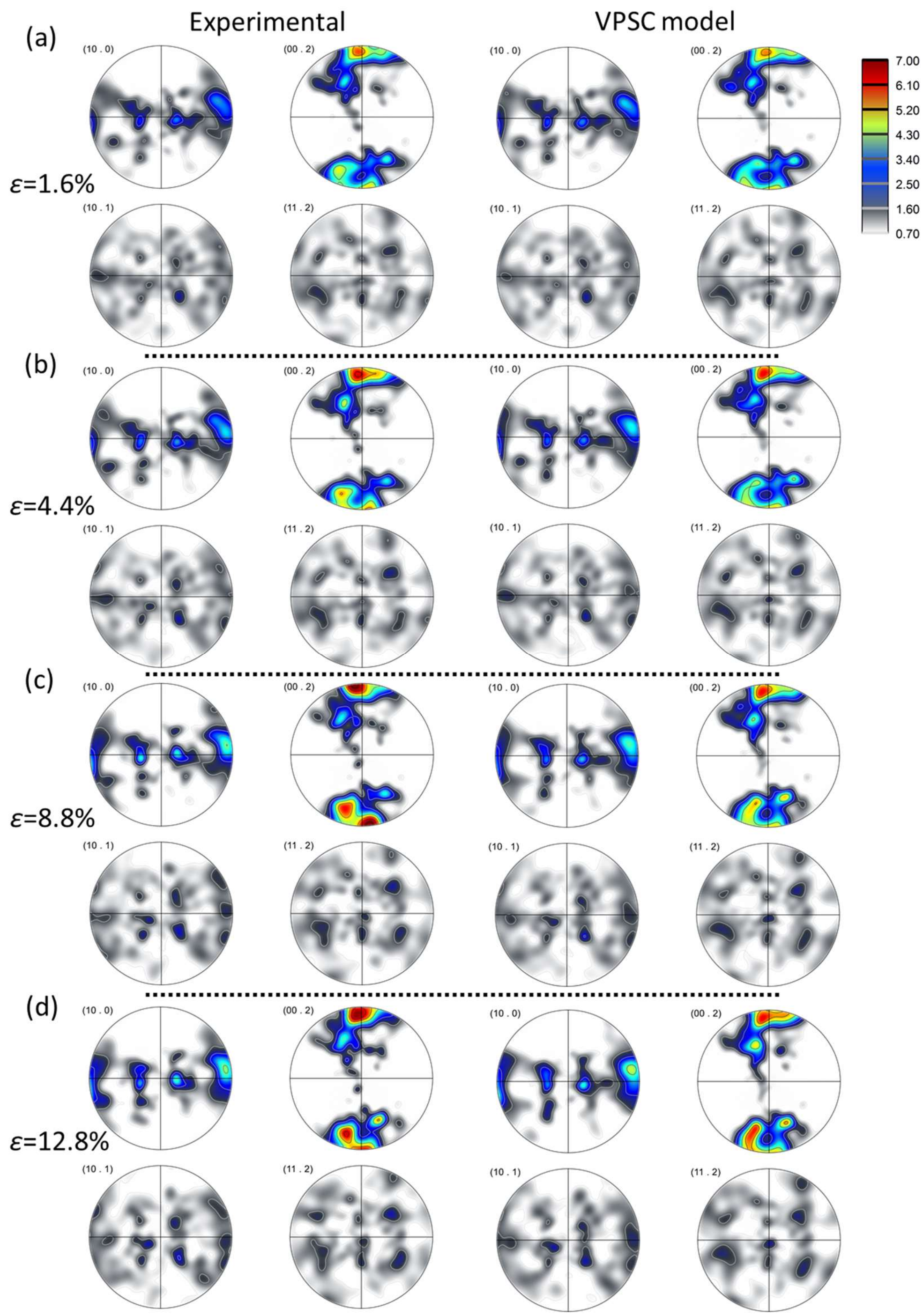

Figure 9. Comparison of the simulated (the left two columns) and the measured (the right two columns) texture for the Mg-Y alloy at (a) 1.6%, (b) 4.4%, (c) 8.8%, and (d) 12.8% strain.

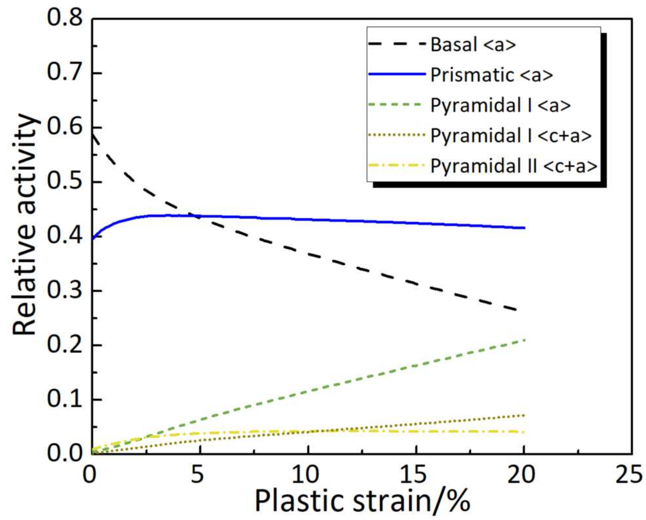

Figure 10. Simulated relative activity plot for the five slip modes of the Mg-Y alloy as a function of the applied strain according to the VPSC simulation.

Fig. 10 provides the simulated relative dislocation activity as a function of plastic strains. The results reveal that the tensile deformation in the early stage (< 1.6% strain) is dominated by the basal 〈a〉 and the prismatic 〈a〉 slip modes, which is consistent with our experimental observation that the basal 〈a〉 and prismatic 〈a〉 slip traces are the dominant slip traces. The simulation also shows that the pyramidal I 〈a〉 dislocation activity noticeably increases and the basal 〈a〉 dislocation activity decreases relatively with increasing deformation strain, but the pyramidal 〈c+a〉 dislocation activity keeps at a very low level during the deformation. This is in agreement with experimental results shown in Fig. 5.

3.4 TEM observation

Ex-situ TEM observation was performed for 9 grains in a Mg-5Y sample with strain of 4%. Based on $\boldsymbol{g}\cdot\boldsymbol{b}$ criterion, where $\boldsymbol{g}$ is diffraction vector and $\boldsymbol{b}$ is Burgers vector of dislocation, it was found that the intragranular deformation of all 9 grains was dominated by 〈a〉 dislocations. Some 〈c+a〉 dislocations were only observed near GBs. Fig. 11 shows a bright-field image of the observed 〈c+a〉 dislocations using a $\boldsymbol{g}$ = 0002 operating reflection close to the $[11\bar{2}0]$ zone axis. The dislocation segment marked by the blue arrow is approximately parallel to the $[10\bar{1}0]$ direction, implying that the 〈c+a〉 dislocation slipped on the pyramidal II plane; the dislocation segment marked by the red arrow has a deviation from the basal plane by ~60°, suggesting that the ⟨c+a⟩ dislocation have slipped on the pyramidal I plane. The L-configuration ⟨c+a⟩ dislocations (7 out of 16 ⟨c+a⟩ dislocations) could be a consequence of the cross-slip of ⟨c+a⟩ dislocation from pyramidal II to pyramidal I plane. Moreover, a close examination of the dislocation segments shows that the pyramidal II ⟨c+a⟩ dislocations are of discontinuous dislocation structures, which indicate that the pyramidal II ⟨c+a⟩ dislocations have dissociated. The pyramidal I ⟨c+a⟩ dislocations do not show such a dissociation phenomenon, which suggests that they have good mobility following cross-slip in the Mg-5Y alloy.

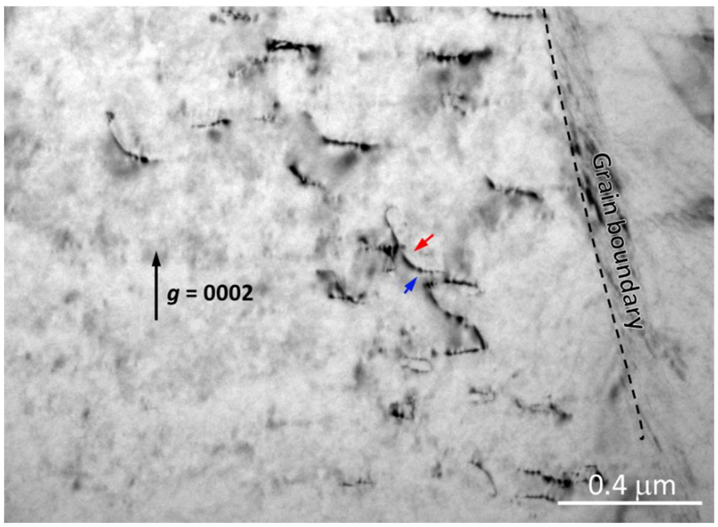

Figure 11. Bright-field image for the ⟨c+a⟩ dislocation cross-slip near GB in the Mg-5Y alloy with a 4% strain, under the $\boldsymbol{g}$ = 0002 diffraction condition near the $[11\bar{2}0]$ zone axis. The dislocation segment marked with the blue arrow could be ascribed to the ⟨c+a⟩ dislocation slipped on the pyramidal II plane. The dislocation marked with the red arrow deviate from the $[10\bar{1}0]$ by ~60°, suggesting cross-slip occurred.

To discover the difference between ⟨c+a⟩ dislocation behavior in Mg alloys with and without rare-earth elements, an extruded Mg-0.47Ca (wt.%) alloy with an 8% tensile strain was studied by TEM as well. Fig. 12 presents a dark-field image of ⟨c+a⟩ dislocations taken along the $[11\bar{2}0]$ zone axis under the $\boldsymbol{g}$ = 0002 operating reflection. Although ⟨c+a⟩ dislocations can also intensively nucleate near GB in the Mg-Ca alloy, a large fraction of the ⟨c+a⟩ dislocations (29 out of 40 ⟨c+a⟩ dislocations) are linear without cross-slip behavior. Moreover, the enlarged area shows that the ⟨c+a⟩

dislocations have dissociated significantly.

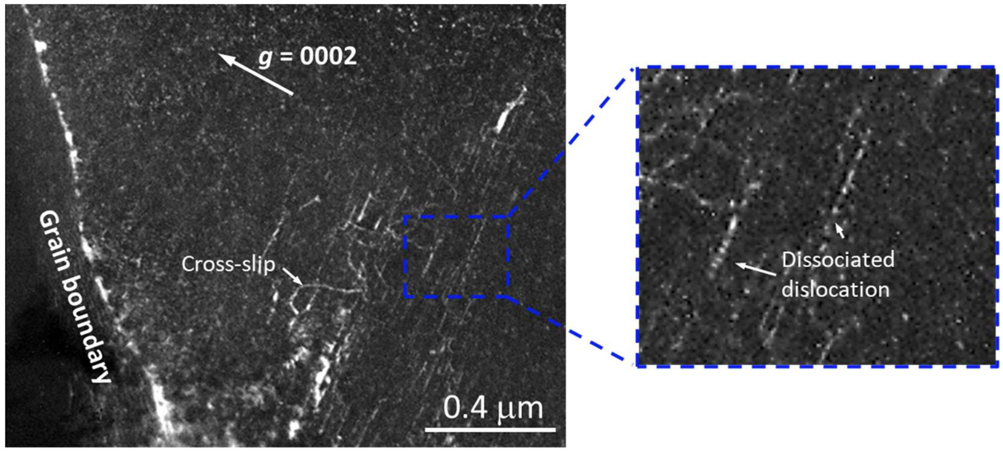

Figure 12. Dark-field image for the ⟨c+a⟩ dislocation cross-slip near GB in the extruded Mg-0.47Ca (wt.%) alloy with an 8% tensile strain, under the $\boldsymbol{g}$ = 0002 diffraction condition near the $[11\bar{2}0]$ zone axis.

4. Discussion

Using the in-situ test in this study, we obtained the CRSSs of different slip modes in the polycrystalline Mg-Y alloy. The CRSS value of basal ⟨a⟩ dislocation slip in the Mg-5Y alloy is estimated as 3 MPa, which is larger than that of the pure Mg (0.52 MPa [41]). An attempt was made to interpret the Y-enhanced $CRSS_{basal\langle a\rangle}$ of the Mg-Y alloy by Labusch model [42]:

$$\Delta\tau = \tau_{alloy} - \tau_{Mg} = Kc^{2/3} \qquad (2)$$

where K is a constant related to the alloying element and temperature, and c is the solute element content, in at. % (~1.3 at.% in this alloy). Based on the K of the element Y (~3 MPa·at$^{-2/3}$) as extrapolated in a recent investigation on the solute strengthening effect in Mg alloys [43], the $\Delta\tau$ is calculated as 3.4 MPa, which indicates that the strengthening effect of Y on basal slip generally follows the strengthening model. Thus, the increase in the $CRSS_{basal\langle a\rangle}$ of the Mg-5Y alloy can be ascribed to solute strengthening.

Reed-Hill et al. [44] reported that the CRSS value of prismatic ⟨a⟩ dislocation slip in pure Mg is ~40 MPa. The $CRSS_{prismatic\langle a\rangle}/CRSS_{basal\langle a\rangle}$ ratio of pure Mg therefore can be calculated as ~80. Based on the measured CRSSs of prismatic ⟨a⟩ and basal ⟨a⟩ dislocation slip in this study, the $CRSS_{prismatic\langle a\rangle}/CRSS_{basal\langle a\rangle}$ ratio of the Mg-5Y alloy is calculated as ~13. This indicates that the addition of Y in Mg does reduce the CRSS ratio between non-basal and basal 〈a〉 slips (from 80 to 13). More interestingly, the CRSS of prismatic <a> in the present alloy is about the same as that of pure Mg alloy. It implies that addition of Y has selectively strengthened the basal <a> dislocation. Furthermore, a significant reduction of CRSS ratio of pyramidal <a> and pyramidal <c+a> to basal <a> dislocation slips, all less than 19, is also achieved in the alloy. All these will contribute to the activation of more non-basal dislocations. In comparison to the relative activities of different dislocation slips in Mg-0.47Ca alloy [add a reference here], the fraction of non-basal dislocation slips in the present alloy is much higher. The difference is especially large for prismatic <a> slips and pyramidal II dislocations. In the Mg-Ca alloy, the fraction of grains with prismatic <a> slips is less than 20% , while no pyramidal II dislocations can be observed at tensile strains less than 8%. It clearly shows the strong effect of Y addition in enhancing non-basal dislocation activities.

It has been argued that the improvement effect of Y on 〈c+a〉 dislocation mobility is a more intrinsic mechanism [12, 14, 18-20] for the high ductility of Mg-Y alloys. Although GBs can enhance the 〈c+a〉 dislocation activity in Mg alloys with or without rare-earth elements due to high stress or strain concentration [39, 45], the activated 〈c+a〉 dislocations in Mg alloys without rare-earth elements have relatively poor mobility. They tend to dissociate into sessile dislocations after nucleation [14], which reduces the ability to relax the stress concentration near GB. Without effective stress relaxation near GBs, the stress concentration would lead to premature fracture. In contrast, the stress concentration could be reduced because of the good mobility of 〈c+a〉 dislocations in Mg alloys with rare-earth elements. The TEM results in the present work does show that the 〈c+a〉 dislocations in the Mg-5Y alloy has higher mobility than that in the Mg-Ca alloy. Such high mobility 〈c+a〉 dislocations, especially those located near GB regions, will help to accommodate deformation strains, reducing the chance of premature facture at GBs. However, since the fraction of <c+a> dislocations is rather low, it is difficult to quantify the contribution of the mobility effect of the dislocations on the total ductility in the alloys.

Conclusions

The dislocation slip behavior in an extruded Mg-5Y alloy was systematically investigated using multi-scale characterization methods. The main results can be summarized as follows:

1. The CRSS values of basal 〈a〉, prismatic 〈a〉, pyramidal I 〈a〉, pyramidal I 〈c+a〉, and pyramidal II 〈c+a〉 dislocation slip in the Mg-5Y alloy were estimated as 3 MPa, 39 MPa, 49 MPa, 57 MPa, and 55 MPa, respectively. The CRSS ratio between prismatic and basal 〈a〉 dislocation slip in the alloy is determined as ~13.
2. Both experimental and simulation results show that the deformation of the Mg-Y alloy was dominated by 〈a〉 dislocations. The non-basal 〈a〉 dislocations shows a relatively high activity during deformation while the contribution of 〈c+a〉 dislocations to the tensile deformation is limited. TEM characterization reveals that the 〈c+a〉 dislocations in Mg-Y alloys have a high mobility due to the ease of cross-slip.
3. The high ductility of Mg-Y alloys has been mainly ascribed to the Y-strengthened basal 〈a〉 slip and the significant reduction CRSS ratio between non-basal dislocations and basal <a> dislocation. The effect of solute Y atoms on mobility improvement of the <c+a> dislocations is also supposed to contribute to thehigh ductility of Mg-Y alloys.

Acknowledgements

This work was financially supported by the National Natural Science Foundation of China (Nos. 51631006 and 51671127) and Qinghai Provincial Science and Technology Key Program (No. 2018-GX-A1). The first author BJZ would like to express his gratitude to the China Scholarship Council (No. 201806230150). We also thank Dr. Carlos N Tomé for help in using the VPSC code.

Reference

[1] U.M. Chaudry, K. Hamad, J.-G. Kim, On the ductility of magnesium based materials: A mini review, J Alloy Compd 792 (2019) 652-664.

[2] B.C. Suh, M.S. Shim, K.S. Shin, N.J. Kim, Current issues in magnesium sheet alloys: Where do we go from here?, Scripta Mater 84-85 (2014) 1-6.

[3] Z. Zeng, N. Stanford, C.H.J. Davies, J.-F. Nie, N. Birbilis, Magnesium extrusion alloys: a review of developments and prospects, International Materials Reviews 64(1) (2019) 27-62.

[4] S. Sandlöbes, S. Zaefferer, I. Schestakow, S. Yi, R. Gonzalez-Martinez, On the role of non-basal deformation mechanisms for the ductility of Mg and Mg-Y alloys, Acta Mater 59(2) (2011) 429-439.

[5] N. Stanford, R. Cottam, B. Davis, J. Robson, Evaluating the effect of yttrium as a solute strengthener in magnesium using in situ neutron diffraction, Acta Mater 78 (2014) 1-13.

[6] D. Zhang, H. Wen, M.A. Kumar, F. Chen, L. Zhang, I.J. Beyerlein, J.M. Schoenung, S. Mahajan, E.J. Lavernia, Yield symmetry and reduced strength differential in Mg-2.5Y alloy, Acta Mater 120 (2016) 75-85.

[7] L.J. Long, G.H. Huang, D.D. Yin, B. Ji, H. Zhou, Q.D. Wang, Effects of Y on the Deformation Mechanisms of Extruded Mg-Y Sheets During Room-Temperature Compression, Metall and Mat Trans A (2020).

[8] K. Takemoto, H. Rikihisa, M. Tsushida, H. Kitahara, S. Ando, Effects of Yttrium Addition on Plastic Deformation of Rolled Magnesium, Mater. Trans. (2020).

[9] L. Tang, W. Liu, Z. Ding, D. Zhang, Y. Zhao, E.J. Lavernia, Y. Zhu, Alloying Mg with Gd and Y: Increasing both plasticity and strength, Comp Mater Sci 115 (2016) 85-91.

[10] J. Hirsch, T. Al-Samman, Superior light metals by texture engineering: Optimized aluminum and magnesium alloys for automotive applications, Acta Mater 61(3) (2013) 818-843.

[11] R. Ahmad, Z. Wu, W.A. Curtin, Analysis of double cross-slip of pyramidal I <c+a> screw dislocations and implications for ductility in Mg alloys, Acta Mater 183 (2020) 228-241.

[12] Z. Wu, R. Ahmad, B. Yin, S. Sandlöbes, W.A. Curtin, Mechanistic origin and prediction of enhanced ductility in magnesium alloys, Science 359(6374) (2018) 447.

[13] K.-H. Kim, J.B. Jeon, N.J. Kim, B.-J. Lee, Role of yttrium in activation of <c+a> slip in magnesium: An atomistic approach, Scripta Mater 108(0) (2015) 104-108.

[14] Z.X. Wu, W.A. Curtin, The origins of high hardening and low ductility in magnesium, Nature 526(7571) (2015) 62-67.

[15] B. Yin, Z. Wu, W.A. Curtin, First-principles calculations of stacking fault energies in Mg-Y, Mg-Al and Mg-Zn alloys and implications for <c+a> activity, Acta Mater 136 (2017) 249-261.

[16] L. Wang, Z. Huang, H. Wang, A. Maldar, S. Yi, J.-S. Park, P. Kenesei, E. Lilleodden, X. Zeng, Study of slip activity in a Mg-Y alloy by in situ high energy X-ray diffraction microscopy and elastic viscoplastic self-consistent modeling, Acta Mater 155 (2018) 138-152.

[17] B. Zhou, L. Wang, W. Liu, J. Wang, X. Zeng, W. Ding, Study of the dislocation activity in a Mg-Y alloy by differential aperture X-ray microscopy, Materials Characterization 156 (2019) 109873.

[18] R. Ahmad, B. Yin, Z. Wu, W.A. Curtin, Designing high ductility in magnesium alloys, Acta Mater 172 (2019) 161-184.

[19] Z. Ding, W. Liu, H. Sun, S. Li, D. Zhang, Y. Zhao, E.J. Lavernia, Y. Zhu, Origins and dissociation of pyramidal <c+a> dislocations in magnesium and its alloys, Acta Mater 146 (2018) 265-272.

[20] Z. Wu, W. Curtin, Mechanism and energetics of<c+a> dislocation cross-slip in hcp metals, Proceedings of the National Academy of Sciences 113(40) (2016) 11137-11142.

[21] R. Ahmad, Z. Wu, S. Groh, W.A. Curtin, Pyramidal II to basal transformation of <c+a> edge dislocations in Mg-Y alloys, Scripta Mater 155 (2018) 114-118.

[22] Z. Huang, L. Wang, B. Zhou, T. Fischer, S. Yi, X. Zeng, Observation of non-basal slip in Mg-Y by in situ three-dimensional X-ray diffraction, Scripta Mater 143 (2018) 44-48.

[23] A. Kula, X. Jia, R.K. Mishra, M. Niewczas, Flow stress and work hardening of Mg-Y alloys, Int J

Plasticity 92 (2017) 96-121.
[24] B. Zhou, L. Wang, P. Jin, H. Jia, H.J. Roven, X. Zeng, Y. Li, Revealing slip-induced extension twinning behaviors dominated by micro deformation in a magnesium alloy, Int J Plasticity 128 (2020).
[25] X. Xu, D. Lunt, R. Thomas, R.P. Babu, A. Harte, M. Atkinson, J.Q. da Fonseca, M. Preuss, Identification of active slip mode in a hexagonal material by correlative scanning electron microscopy, Acta Mater 175 (2019) 376-393.
[26] T.R. Bieler, R. Alizadeh, M. Peña-Ortega, J. Llorca, An analysis of (the lack of) slip transfer between near-cube oriented grains in pure Al, Int J Plasticity 118 (2019) 269-290.
[27] C.J. Boehlert, Z. Chen, I. Gutiérrez-Urrutia, J. Llorca, M.T. Pérez-Prado, In situ analysis of the tensile and tensile-creep deformation mechanisms in rolled AZ31, Acta Mater 60(4) (2012) 1889-1904.
[28] B. Zhou, L. Wang, W. Liu, X. Zeng, Y. Li, Revealing the Subsurface Basal 〈a〉 Dislocation Activity in Magnesium Through Lattice Rotation Analysis, Metall and Mat Trans A (2020).
[29] B. Hutchinson, J. Jain, M.R. Barnett, A minimum parameter approach to crystal plasticity modelling, Acta Mater 60(15) (2012) 5391-5398.
[30] Q. Chen, L. Hu, L. Shi, T. Zhou, M. Yang, J. Tu, Assessment in predictability of visco-plastic self-consistent model with a minimum parameter approach: Numerical investigation of plastic deformation behavior of AZ31 magnesium alloy for various loading conditions, Materials Science and Engineering: A 774 (2020).
[31] C. Zhao, X. Chen, F. Pan, J. Wang, S. Gao, T. Tu, C. Liu, J. Yao, A. Atrens, Strain hardening of as-extruded Mg-xZn (x = 1, 2, 3 and 4 wt%) alloys, J Mater Sci Technol 35(1) (2019) 142-150.
[32] T. Nakata, J.J. Bhattacharyya, S.R. Agnew, S. Kamado, Unexpected influence of prismatic plate-shaped precipitates on strengths and yield anisotropy in an extruded Mg-0.3Ca-1.0In-0.1Al-0.2Mn (at.%) alloy, Scripta Mater 169 (2019) 70-75.
[33] K.-H. Kim, K. Okayasu, H. Fukutomi, Influence of the Initial Texture on Texture Formation of High Temperature Deformation in AZ80 Magnesium Alloy, Mater. Trans. 56(1) (2015) 17-22.
[34] S.R. Agnew, C.N. Tomé, D.W. Brown, T.M. Holden, S.C. Vogel, Study of slip mechanisms in a magnesium alloy by neutron diffraction and modeling, Scripta Mater 48(8) (2003) 1003-1008.
[35] M. Jahedi, B.A. McWilliams, P. Moy, M. Knezevic, Deformation twinning in rolled WE43-T5 rare earth magnesium alloy: Influence on strain hardening and texture evolution, Acta Mater 131 (2017) 221-232.
[36] M. Lentz, M. Risse, N. Schaefer, W. Reimers, I.J. Beyerlein, Strength and ductility with {10-11}-{10-12} double twinning in a magnesium alloy, Nat Commun 7 (2016) 11068.
[37] L.J. Long, G.H. Huang, D.D. Yin, B. Ji, H. Zhou, Q.D. Wang, Effects of Y on the Deformation Mechanisms of Extruded Mg-Y Sheets During Room-Temperature Compression, Metall and Mat Trans A 51(6) (2020) 2738-2751.
[38] G. Zhu, L. Wang, H. Zhou, J. Wang, Y. Shen, P. Tu, H. Zhu, W. Liu, P. Jin, X. Zeng, Improving ductility of a Mg alloy via non-basal <a> slip induced by Ca addition, Int J Plasticity 120 (2019) 164-179.
[39] J. Koike, R. Ohyama, Geometrical criterion for the activation of prismatic slip in AZ61 Mg alloy sheets deformed at room temperature, Acta Mater 53(7) (2005) 1963-1972.
[40] J. Yang, Z.M. Song, L.M. Lei, G.P. Zhang, Detecting mechanical properties of microstructure units in Ti-6.5Al--3.5Mo--1.5Zr--0.3Si alloy, Materials Science and Engineering: A 617 (2014) 84-88.
[41] H. Conrad, W. Robertson, Effect of temperature on the flow stress and strain-hardening coefficient of magnesium single crystals, Jom-Us 9(4) (1957) 503-512.

[42] R. Labusch, A Statistical Theory of Solid Solution Hardening, physica status solidi (b) 41(2) (1970) 659-669.
[43] A. Tehranchi, B. Yin, W.A. Curtin, Solute strengthening of basal slip in Mg alloys, Acta Mater 151 (2018) 56-66.
[44] R.E. Reed-Hill, W.D. Robertson, Deformation of magnesium single crystals by nonbasal slip, Jom-Us 9(4) (1957) 496-502.
[45] J. Koike, T. Kobayashi, T. Mukai, H. Watanabe, M. Suzuki, K. Maruyama, K. Higashi, The activity of non-basal slip systems and dynamic recovery at room temperature in fine-grained AZ31B magnesium alloys, Acta Mater 51(7) (2003) 2055-2065.